IEEE Access
Multidisciplinary ⋮ Rapid Review ⋮ Open Access Journal

Received July 2, 2020, accepted August 1, 2020, date of publication August 6, 2020, date of current version August 18, 2020.

Digital Object Identifier 10.1109/ACCESS.2020.3014700

Multichannel W-Band SAR System on a Multirotor UAV Platform With Real-Time Data Transmission Capabilities

SUMIN KIM[1], (Graduate Student Member, IEEE), SE-YEON JEON[1,2], (Member, IEEE), JEONGBAE KIM[1], (Graduate Student Member, IEEE), UI-MIN LEE[1], SEUNGHA SHIN[3], YOUNGWOO CHOI[3], AND MIN-HO KA[1], (Member, IEEE)

[1]School of Integrated Technology, Yonsei University, Seoul 21983, South Korea
[2]Microwaves and Radar Institute, German Aerospace Center (DLR), 82234 Bayern, Germany
[3]U-Tel Company Ltd., Gunpo 15880, South Korea

Corresponding author: Min-Ho Ka (kaminho@yonsei.ac.kr)

This work was supported by the Specialized Research Center for Next Generation Synthetic Aperture Radar, originally funded by the Defense Acquisition Program Administration (DAPA) and Agency for Defense Development (ADD), South Korea, under Grant 2019-09-007.

ABSTRACT In recent years, the demand for small-scale remote sensing, which is used in disaster monitoring, agriculture, and ground subsidence has increased. A multichannel synthetic aperture radar (SAR) system can provide image and topographic information of the illuminated scene, regardless of adverse weather conditions. As a cost-effective solution to radar imaging, a multichannel W-band SAR system mounted on a multirotor unmanned aerial vehicle (UAV) is presented. The radar module was designed to operate at W-band to achieve small size and weight allowing the module to be mounted on multirotor UAVs with small payload. A detailed description of the design and measurement of the system is provided in this paper. The radar imaging capability of the developed system was verified by performing outdoor experiments using isolated buildings as targets. The multichannel functionality of the system was verified by measuring height of a point target placed above the ground. The measurements and experiments verified the feasibility of a multichannel radar mounted on a multirotor UAV for imaging and topographic applications.

INDEX TERMS Synthetic aperture radar, unmanned aerial vehicles, W-band radar, multichannel radar, interferometry.

I. INTRODUCTION

The applications of multirotor unmanned aerial vehicles (UAV) have increased in civil and industrial fields in the past few decades [1]. An in-depth survey of the multirotor UAVs used in civil and industrial fields, such as search and rescue, remote sensing, construction and infrastructure inspections, precision agriculture, delivery of goods, monitoring of road traffic, and surveillance is given in [1]. In the remote sensing field, multirotor UAVs are considered an effective sensor platform for small-area remote sensing compared to traditional satellite and airborne platforms. The use of drones in applications, such as precision agriculture [2], coastal and polar monitoring [3]–[5], disaster and emergency monitoring [6], and atmospheric monitoring [7], is a common and mature methodology. The potential and novel applications of UAVs in remote sensing applications, including urban planning and management, engineering monitoring, ecological and environmental monitoring, archeology and cultural heritage sites, and human and social understanding, are well assessed in [8].

The sensors mounted on multirotor UAVs are typically optical sensing instruments [9]; however, various imaging and ranging instruments are available from near infrared [10] to thermal infrared and microwave. Ranging instruments in the microwave region, referred to as radars, are advantageous owing to their ability to retrieve range and velocity information in adverse conditions. A survey on radars mounted on multirotor UAVs is provided in [11] along with an experimental result of multiple-input multiple-output (MIMO) imaging radar mounted on a hexacopter. UAV-borne radars were used

The associate editor coordinating the review of this manuscript and approving it for publication was Yue Cao.

as an altimeter in [12], [13] to aid drone maneuverability and provide increased flight safety. A 26 *GHz* radar was also used as an altimeter in [14] to generate a terrain map of the experiment scene. Moses proposed an X-band radar mounted on a drone in [15] for collision avoidance in a realistic scenario. The use of radars mounted on drones for glaciology [16] and soil moisture mapping [17] has also shown to be effective.

Among the numerous applications of radars, synthetic aperture radar (SAR) systems have become an extraordinary tool for remote sensing [18]. SAR systems utilize the movement of the platform relative to the illuminated scene to synthesize the image of the targets and clutter within the antenna footprint. More than a dozen active satellite-borne SAR systems and numerous airborne SAR systems for various types of airborne platforms have been proven successful for earth observations [19]. While a conventional SAR measures the location of the target in a two-dimensional coordinate system, multiple SAR images can be coherently exploited to obtain additional information of the illuminated scene [20]. This technique is called SAR interferometry (InSAR) and is utilized for topographic mapping and motion mapping of the illuminated scene.

The traditional SAR systems mounted on satellites or manned aircrafts are not suitable for quick acquisition of data, ultrahigh spatial resolution, and small-area remote sensing [8]. An alternative to the traditional platform introduced to the field of SAR systems is the UAV platform. The technical challenge to the platform change was reducing the size of the bulky radar systems to board them on UAVs, which have a small payload compared to that of traditional platforms. Numerous reports on SAR systems mounted on winged UAVs [21]–[25] and multirotor UAVs [26]–[31] have been published in the past two decades. Multirotor UAVs, compared to winged UAVs, are advantageous in civil applications owing to their easy-to-operate, easy-to-deploy, low-cost, and vertical take-off and landing characteristics [1]. However, until recently, because of their unstable flight and low payload, the multirotor platforms have not been exploited for SAR platforms.

In [27], an X-band frequency modulated continuous wave (FMCW) radar sensor was developed for a multicopter UAV platform, and various SAR experiments were conducted. The phase error owing to the non-ideal motion of the platform was compensated using passive active radar calibrators located within the antenna footprint. Thus, polarimetric SAR images were obtained by alternating transmit antennas, and interferometric SAR images were obtained by a repeat-pass SAR experiment. In [28], a near-real time motion compensation technique was used to generate a SAR image using a multicopter UAV. In [29], a downward looking ground penetrating radar mounted on a multicopter UAV platform was introduced. Metal objects buried under ground were used as the target scene, and the locations of the hidden objects were retrieved by synthesizing the SAR image. In [30], a commercial low cost ultra wide band pulse radar was mounted on a multicopter drone to generate a SAR image of metallic objects.

In this study a multichannel W-band SAR system mounted on a multirotor UAV platform, addressed as Drone SAR system in this paper, was evaluated. A single input multiple output (SIMO) FMCW radar architecture was adopted for simple implementation of a multichannel radar system. The W-band frequency was used for the transmit signal to minimize the size and weight of the hardware. Commercial monolithic microwave integrated circuits (mmICs) were used to develop the W-band RF board for minimizing size and weight of the hardware. Commercial datalink at the ISM bands was used to lower the development costs and minimize the size and weight of the system. A hexatrotor UAV equipped with a navigational system was chosen for the platform. A gimbal was adopted to minimize the vibrational effects caused by unwanted platform movement or sudden atmospheric disturbances.

The developed system differs from previous research on multirotor UAVs based on two unique characteristics: the real-time online data transmission capability, and the multichannel data acquisition capability.

Real-time data acquisition allows real-time generation of radar images when combined with adequate SAR algorithms and processors. The acquired images can be used for real-time monitoring and remote sensing. Real-time monitoring is essential in UAV applications for time-critical events, such as emergency disasters, industrial inspection, military events, etc. [32]. The real-time capability is also beneficial when the UAV is entering a dangerous area. When a UAV enters a dangerous area the vehicle may not recover, which could result in the loss of captured data if the user cannot acquire the data in real-time.

A multichannel SAR system is used for wide swath high resolution imaging, moving target indication, and height estimation. Considering the UAV-borne SAR systems used for small scale remote sensing, moving target indication and height estimation was considered a useful application for UAV-borne SAR systems. The multichannel data acquired simultaneously from two different antennas can be coherently exploited to perform single-pass InSAR measurements. The InSAR measurements can be exploited to obtain topographic information or moving target information of the SAR image.

The system performance of the presented system was validated through field tests at Yonsei University, Republic of Korea. The radar imaging performance was verified by illuminating an isolated building and synthesizing a radar image. The radar imaging was further analyzed by performing an experiment using corner reflectors. The utility of the SIMO architecture was validated by performing an InSAR experiment on a flat surface with a corner reflector of a known height. The relative height of the corner reflector was measured from the interferometric SAR images generated by two channels separated in the height direction, and this method was confirmed to be effective.

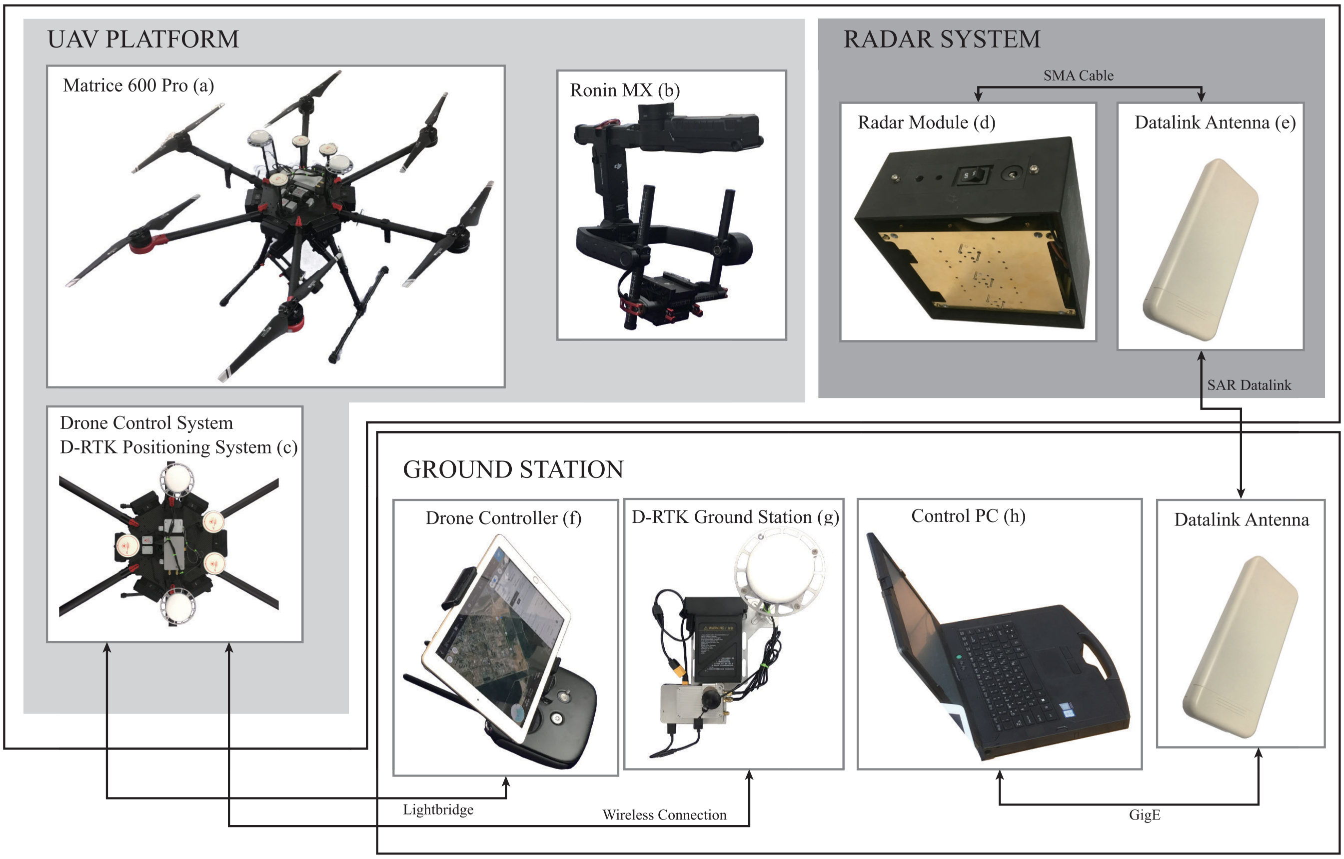

FIGURE 1. General overview of the SAR system with pictures of each subsystems.

The manuscript is organized as follows. Section II shows the hardware elements used for the Drone SAR system. This section covers the design, choice of hardware, and implementation issues regarding the whole system. Section III describes SAR data acquisition of different targets and data processing. The data acquisition includes data from artificial targets and corner reflector of a known height. The data processing includes motion compensation, SAR image formation, and InSAR processing. Section IV concludes the manuscript with summarization of our findings.

II. SYSTEM DESIGN AND IMPLEMENTATION

This section details the characteristics of the hardware elements used for the Drone SAR system. The system consists of three subsystems; the UAV platform, radar system, and ground station. Each subsystems are further divided into independent hardware modules which are shown in Figure 1.

Table 1 shows the system requirements for the proposed Drone SAR system. W-band frequency was used to design the SAR system to minimize the size and weight of the radio frequency (RF) hardware. 77 GHz radar sensors are widely available on the market due to the advancing evolution of automotive radar sensors, thus was chosen for the center frequency [33]. Considering small scale remote sensing applications, the resolution requirement was chosen to be 20 cm.

TABLE 1. SAR system requirements.

Parameters	Units	Value
center frequency	GHz	77
number of Tx channels	-	1
number of Rx channels	-	2
resolution	cm	20
target range	m	100
platform	-	multirotor UAV

A. UAV PLATFORM

The functionality of the platform in a SAR system is to move the radar so that the target scene is illuminated at different angles. An ideal movement of the platform is a linear trajectory of a constant velocity without vibrations, which is difficult to achieve with a lightweight UAV flying at a low altitude. To perform SAR experiments under adverse circumstances, a six-rotor UAV designed for professional photography and industrial applications in conjunction with a gimbal and real time kinetics (RTK) system was used. The model names of the UAV, gimbal, and RTK system were Matrice 600 Pro [34]

(Figure 1 (a)), Ronin-MX [35] (Figure 1, (b)), and D-RTK [36] (Figure 1 (c)), all were manufactured by DJI.

Matrice 600 Pro, shown in Figure 1, is equipped with six carbon fiber propellers, six intelligent flight batteries, an A3 Pro flight control system, a DJI Lightbridge 2 air system, and two DJI Lightbridge 2 air system antenna [34]. A3 Pro is a flight control system designed by DJI for a wide range of multirotor UAVs to realize accurate attitude control and high-precision position of the aircraft [37]. The system includes a three GPS-Compass Pro module, three IMU-Pro module, and power management unit (PMU). The flight control system works in conjunction with the DJI Lightbridge 2 system to control and maneuver the platform [38]. The DJI Lightbridge 2 is a long-range video downlink for transmitting video and is composed of an air system module and a ground system. The UAV weighs 10 *kg* with batteries, and its dimensions are 1668 *mm* × 1518 *mm* × 727 *mm*.

Precise platform positioning and heading is important for SAR systems. Inaccurate movement of the platform manifests in the SAR signal as a phase error. In addition, the angle between the radar line of sight and the platform movement is one of the most important factors when synthesizing SAR images. This angle determines the squint angle of the SAR measurement which determines the Doppler centroid of the SAR signal. To precisely control and stabilize the heading and movement of the platform during the SAR experiment, the D-RTK system was adopted. The D-RTK system is a GPS and barometer system designed to provide accurate positioning and heading [36]. The system consists of two D-RTK processors and three GNSS antennas, where one processor and two GNSS antennas are placed on the platform and the others are used as a fixed base station on the ground. The Matrice 600 Pro combined with the D-RTK system provides 1 *cm* of horizontal position accuracy, 2 *cm* of vertical position accuracy, 0.4° of orientation accuracy, and 0.03 m/s of speed root mean square.

The vibration caused by the propellers and wind manifests as phase errors in the SAR signal, thus the radar system was mounted on the Ronin-MX Gimbal to minimize it's effects. The Ronin-MX, originally designed for filming cameras, is easily integrated to general cameras using the camera mount plate included in the product. Therefore, the radar system was designed to have dimensions similar to that of a general camera for easy integration with the gimbal. With the radar mounted on the gimbal, the roll angle is directly related to the depression angle of the antenna, which determines the antenna footprint in a SAR measurement. The control of the gimbal roll angle was possible using the DJI Lightbridge 2 remote controller, which was used to control the antenna footprint.

B. RADAR SYSTEM

In SAR systems, the antennas have the largest contribution to the payload of the platform. Because of the small size and payload of the multirotor UAV platform, the goal of the radar system design was to minimize size and weight. Therefore, the W-band frequency was chosen to minimize the size and weight of the antenna and RF components.

TABLE 2. Radar system requirements.

	Parameters	Units	Value
Transmitter	center frequency	GHz	77
	bandwidth	GHz	1
	transmitted power	dBm	20
	power flatness	dB	±2
Receiver	input frequency	GHz	77 ± 0.5
	receive gain	dB	35
	channel gain deviation	dB	±1.5
Total	weight	kg	3
	size	cm^3	$10,000$

Multichannel radars provide an opportunity to extract height information or moving target information from a single SAR measurement. To maintain the small size and weight of the radar system while implementing a multichannel radar, a SIMO radar architecture with one transmit (Tx) antenna and two receive (Rx) antennas was chosen for the radar system.

A UAV can be used for remote sensing to investigate hazardous areas without risking human resources. Hazardous areas threaten the platform flight and the platform may not be able to return after the remote sensing mission. To preserve the data under the risk of losing the platform, real-time raw data transmission capability is essential, which was considered when designing this radar system.

Considering the above, the radar system requirements were defined as Table 2 to meet the SAR system requirements [39], [40]. The radar system (Figure 1 (d)) was designed with three main boards; the RF board, digital board, and datalink board. A picture and functional diagram of each boards are shown in Figure 2. In Figure 2, the physical location corresponding to the function described in the diagram is marked with a letter.

1) RF BOARD

To minimize the size and weight of the radar module, W-band of 77 *GHz* was chosen for the radar center frequency. Moreover, commercial W-band monolithic mmIC chips were used to further reduce the size and weight of the radar system, which alleviates the burden of power consumption, size, and weight that is introduced when designing a radar transceiver from individual elements.

The Tx waveform used in the RF module is a sawtooth FMCW. When a sawtooth voltage ramp is input from the digital board to the voltage controlled oscillator (VCO) mmIC (Figure 2 (a)) an X-band linear frequency modulated signal from 9.625 *GHz* − 67.5 *MHz* to 9.625 *GHz* + 67.5 *MHz* is generated. The signal is then divided and transferred to the transmitting mmIC and two receiving mmICs (Figure 2 (b) and (c)). The Tx mmIC chip upconverts the signal to the W-band by an eight-time multiplier and amplifies the signal resulting in a W-band signal with a frequency of 77 *GHz*±1 *GHz* and power greater than 20 *dBm*. The

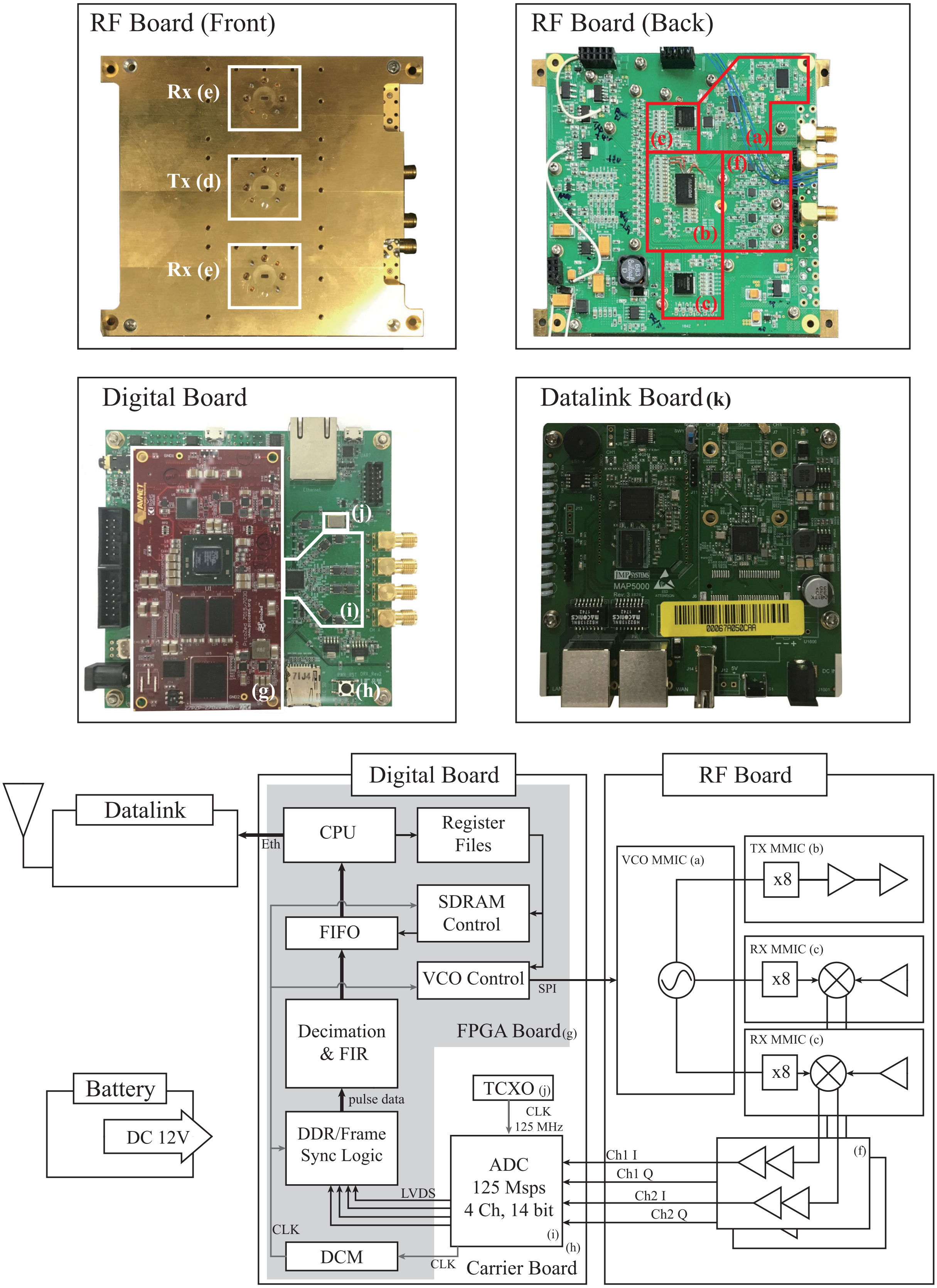

FIGURE 2. Picture of the RF board, digital board, and datalink board (top) and functional diagram of the radar system (bottom).

W-band signal is then transferred to the Tx antenna via a WR-12 waveguide port located on the back side of the RF board (Figure 2 (d)).

When receiving the backscattered signal, the radar module uses deramp on receive to convert the RF signal into an intermediate frequency (IF) signal. The backscattered signal received from two Rx ports (Figure 2 (e)) are transferred to Rx mmIC chips (Figure 2 (c)). The Rx mmIC chips mix the received signal with a reference W-band signal, which are generated within the Rx chip using the X-band signal received from the VCO. The output of the Rx mmICs goes through a chain of IF low-noise amplifiers (Figure 2 (f)) to enhance the signal quality. Two in-phase signals, Ch1 I and Ch2 I, and two quadrature-phase signals, Ch1 Q and Ch2 Q, are then transferred to the digital board for digitization and to-ground transmission.

The RF board functionalities were measured using a signal analyzer and power meter. The transmitted power was measured using an Agilent N1911A power meter, an RF power meter measuring instrument that can measure up to 100 *GHz*. The Tx port of the RF board was connected to the power meter for the test. To operate the RF board on a single tone mode, a VCO control board was connected to the RF board. The measured power of the transmitted signal resulted in 21.67 *dBm*.

To test the bandwidth of the transmitted signal, a signal analyzer, Keysight E4440A, was combined with a harmonic mixer, Keysight 11970W. The harmonic mixer is an auxiliary component that is used for measuring W-band devices with Keysight E4440A. Figure 3 (a) shows the schematic and a picture of the RF board under a transmit signal bandwidth test. A 40 *dB* attenuator was attached to the Tx port of the RF board prior to the harmonic mixer to protect the measuring instrument. The output of the harmonic mixer was connected to the signal analyzer via SMA cables. The RF board was operated to transmit LFM signals from 76.3 *GHz* to 77.7 *GHz*.

The measured amplitude versus frequency from the signal analyzer is shown in Figure 3 (c). The frequency range required for the transmitter is from 76.5 *GHz* to 77.5 *GHz*, shaded gray in the figure. Figure 3 (c) shows that the RF board is capable of transmitting a bandwidth of 1 *GHz* centered at 77 *GHz*. The amplitude deviation within the frequency range is 3.37 *dB*, which is appropriate for FMCW SAR experiments.

To test the receiver gain, a W-band source module, Agilent 510MS-AG, was utilized. The W-band source module was connected to the Rx port of the RF board, and the IF signal port was connected to the signal analyzer, Keysight E4440A. To provide a reference signal to the RF mmIC chip, the transmitter was set to run in CW mode using the VCO control board. To remove the interference from the Tx port, a terminator was connected to the Tx port. A picture and schematic of the receiver test are shown in Figure 3 (b). The power of the signal from the W-band source module was 7 *dBm*. To protect the IF amplifiers within the RF board, a 50 *dB* attenuator was attached prior to the Rx port; thus, the power of the input signal to the RF board equaled −43 *dBm*. To test the receiver gain, the spectrum analyzer was connected to Ch 1 of the IF port when the source module was connected to Rx 1 port, and when the spectrum analyzer was connected to Ch 2, the source module was connected to Rx 2. The single-tone signal measured from the signal analyzer is shown in Figure 3 (d), where the blue line depicts the signal from Ch 1, and the red line depicts the signal from Ch 2. The receiver gain is calculated by (1), where G_{Rx} is the receiver gain, P_{input} is the power of the W-band signal input to the Rx port, and P_{IF} is the amplitude of the single tone signal measured from the signal analyzer. The resultant IF powers measured using (1) are 34.29 *dB* and 35.52 *dB* for Rx 1 and Rx 2, respectively.

$$\begin{aligned} G_{RX} &= P_{IF} - P_{input} \\ &= P_{IF} + 43\ dBm \end{aligned} \tag{1}$$

2) DIGITAL BOARD

The digital board has five main functions. The first initializes the VCO mmIC and analog to digital converter (ADC). The second achieves coherency between transmission and digitization of the radar signal, and the third digitizes the IF signals received from the RF board. The fourth synchronously stores the digitized radar data to memory synchronously with the PRI and the fifth transfers the digital data to the datalink board. To realize these functions, while maintaining a small size, weight, and power consumption, the digital board was designed using a commercial field-programmable gate array (FPGA) board (Figure 2 (g)) and carrier board (Figure 2 (h)).

The FPGA board used for the digital board was PicoZed manufactured by AVNET [41]. PicoZed is a flexible system-on-module with common functions, such as memory, Ethernet, serial peripheral interface, etc, integrated on a single board. PicoZed is based on Zynq-7000 all programmable system-on-chip (SOC) manufactured by Xilinx [42]. Zynq-7000 is a product that includes a dual ARM Cortex-A9 (a 32-bit processor) processing system (PS) and Xilinx programmable logic (PL) in a single chip.

The carrier board includes an ADC, temperature constant crystal oscillator (TCXO), and multiple connectors. The connectors include SMA connectors for receiving IF signals, pin header connectors for the serial peripheral interface (SPI), a gigabit Ethernet port for connection to the datalink board, and a PicoZed mezzanine connector to connect to PicoZed.

The ADC digitizes the IF signals (Figure 2 (i)) on the carrier board. The ADC receives the IF signals and a 125 *MHz* clock signal (CLK) from the TCXO (Figure 2 (j)) and outputs four low-voltage differential signals (LVDSs). The LVDSs transferred to the FPGA board are transformed into FPGA internal signals. A clock signal synchronous to the ADC sampling is also transferred to the digital clock manager (DCM) implemented within the PS to manage the transmitter control and to-memory data transfer synchronously with the ADC sampling.

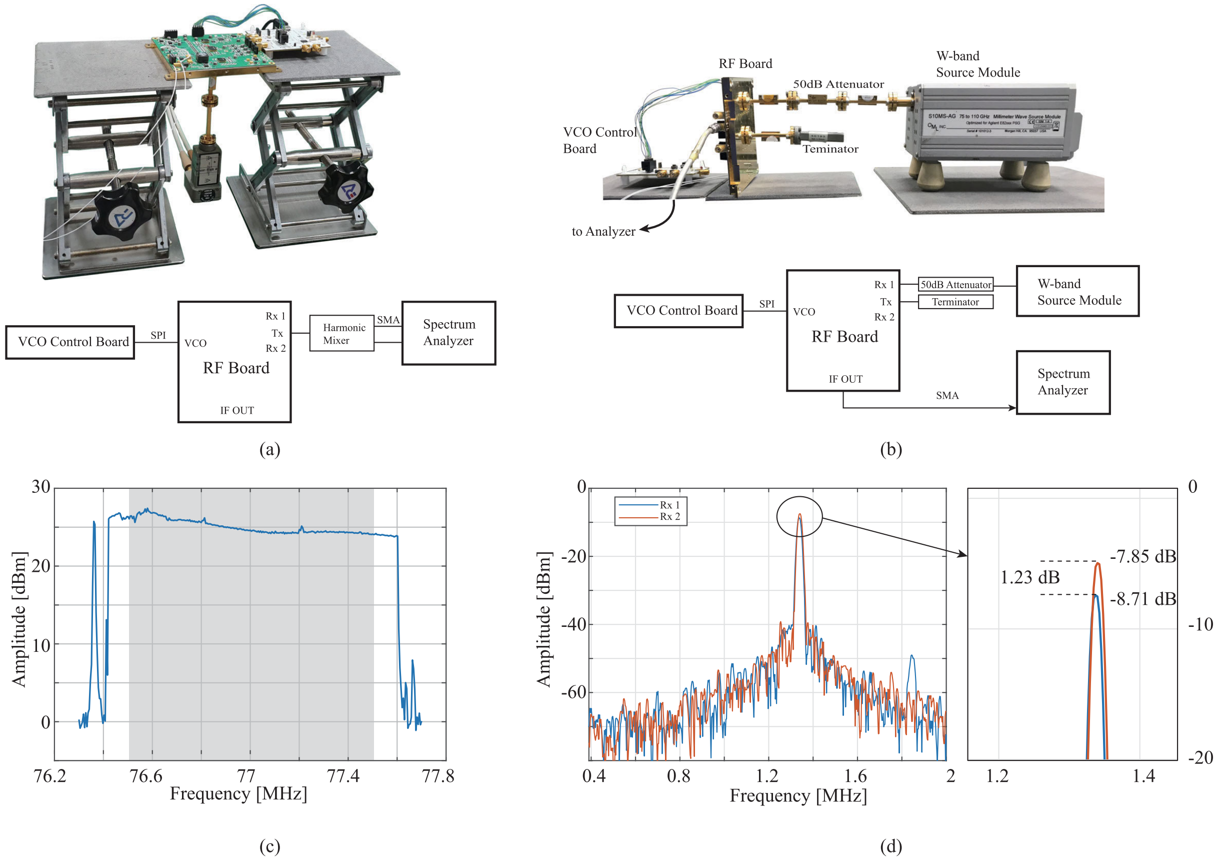

(a)

(b)

(c)

(d)

FIGURE 3. RF board performance test. Image (a) is a picture and schematic of the Tx bandwidth test; (b) is a picture and schematic of the Rx gain test; (c) shows the result of the Tx bandwidth test, and (d) shows the result of the Rx gain test.

The logics implemented using the PL of the FPGA board include DCM, double-datarate (DDR)/Frame Sync Logic, Decimation & finite impulse response (FIR), synchronous dynamic random access memory (SDRAM) Control, and VCO Control. The logics operate synchronously with the CLK generated by the DCM. The DDR/Frame Sync Logic transforms the LVDS signal into FPGA internal signals. The internal signals are transferred to the Decimation & FIR to be decimated by a factor of 50. When the VCO Control is activated, the module periodically sends SPI signals to the VCO mmIC to activate the transmitter. Simultaneously, the SDRAM Control is activated to transfer the decimated data to the FIFO within the memory via direct memory access (DMA).

The PS within the FPGA board works as a bare metal computer with an application to control the PL running on it. Upon powering on the digital board, the PS initializes the VCO and the ADC via a SPI signal route connected to the serial data input of the VCO mmIC and ADC. Then, a TCP/IP server is opened to be connected to the ground station. When the connection is established, the PS activates the PL logics by changing the values within the register files according to the commands received from the ground station. The commands include changing the VCO settings, activating the VCO Control, and activating the SDRAM Control.

The PS also sends the digitized data to the datalink board via the gigabit Ethernet port installed on the carrier board. When the server application receives a command to turn on the network function, the PS reads the pulse data from the memory and frames the digital data into user defined packets (UDP). The UDP are then transferred to the Ethernet port to be transferred to the datalink board.

The digital board was assembled by using a fabricated board, which includes ADC, TCXO, a gigabit Ethernet port, SMA connectors, and the commercial FPGA board. The board was designed to operate with an input voltage of 12 V DC. The overall size of the digital board was 110 $mm \times 110$ mm, and the measured power consumption was 4 W.

3) DATALINK BOARD

The datalink board (Figure 2 (k)) transfers commands from the ground station to the digital board and transmits the UDP packets received from the digital board to the ground station via 2.4GHz wireless interface. To reduce the development costs, commercial wireless equipment for the outdoors, shown in Figure 4 (a), was used. For a compact design of the radar module, the modem was separated from the wireless equipment and was placed inside the radar module case along with the RF and digital board. A 2 × 2 bidirectional patch

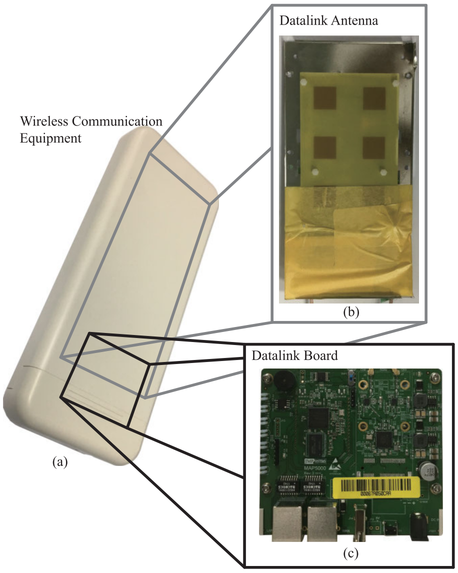

FIGURE 4. **Picture of the wireless equipment, datalink board, and datalink antenna. Image (a) shows the wireless equipment in a plastic case; (b) shows the two 2 × 2 patch antenna used for the datalink, and (c) is a picture of the datalink board.**

antenna with a gain of 17 dBi, shown in Figure 4 (b), was used for the datalink antenna. The datalink utilizes an ISM band of $5180 - 5805$ MHz with a bandwidth of 80 MHz. The overall size of the datalink board was 110 $mm \times 110$ mm, and the power consumption was 4 W.

The RF, digital, and datalink boards were stacked into a single module using PCB supports and via holes that were designed to fit each other. The assembled radar module was powered by a commercial 12 V cylindrical cell Lithium-ion battery. A case was designed using lightweight plastic to protect the three main boards, power, and connection cables, shown in Figure 5 (a). The bottom of the case was designed to mount the commercial camera. The camera mount was then mechanically attached to the gimbal to affix the radar module to the UAV platform. The datalink antenna was attached to the gimbal to direct the ground station. The power consumption, dimension, and weight of the radar module were measured to be 25.6 W, 130 $mm \times 130$ $mm \times 62$ mm, and 0.766 kg, respectively.

C. GROUND STATION

The ground station is composed of a ground station datalink, control PC (Figure 1 (h)), and drone control units (Figure 1 (f) and (g)).

1) GROUND STATION DATALINK

The same wireless equipment used in the datalink was used for the ground station datalink to remotely communicate with the radar system. The ground station datalink was connected to the control PC via gigabit Ethernet. Upon powering on the radar module and the ground station datalink, the datalink tests for the connection between the two remote modems and notifies the users with a loud beep when the connection is established. Then, the ground station datalink may receive commands from the control PC and transfer them to the radar system. The ground station datalink is also responsible for transferring raw data received from the radar module to the control PC.

2) CONTROL PC

The control PC was responsible for setting the experiment mode, starting the radar signal transmission, and storing the raw data to storage. To set the experiment mode, the control PC connects to the server application running on the radar system via TCP/IP. A set of commands are available on the application, which can be utilized by sending predesignated command codes, including setting the PRI value, turning the PRI on or off, turning the network function on or off, etc.

A data conversion software to store the raw data was developed. The data of a single ramp are too large to be framed into a single UDP packet; thus, a single pulse was divided into four UDP packets and were sent to the ground station. When the UDP packets are received from the datalink to the data conversion software, the software looks for four packets that belong to the same pulse and combines them into a single 16 KB file. The information within the file includes the amplitude of the four IF signals and the transmission time of the pulse. To reduce the data size, the difference of the transmission time between pulses rather than an absolute time were included in the datafile.

3) DRONE CONTROL UNIT

The drone control unit consists of a DJI Lightbridge 2 remote controller, tablet, and DJI-RTK ground unit. The DJI-RTK ground unit consists of a processor and GNSS antenna and is located near the flight area in a fixed position on the ground throughout the flight.

The DJI Lightbridge 2 remote controller is used to communicate with the Lightbridge 2 air system on the platform to control the UAV movements. The angle between a horizontal plane parallel to the ground and the radar LOS is called the depression angle. The angle in conjunction with the platform altitude determines the antenna footprint for a given antenna radiation pattern. The roll angle of the gimbal determines the depression angle, which is controlled by the remote controller.

An iPad, manufactured by Apple, was used for the tablet to launch the applications provided by DJI. The application named DJI Go was used to check the initial status of the UAV and to set the gimbal operation mode [43]. Before taking off, the initial status, such as battery life, GNSS connection, and DJI-RTK connection, should be checked. The gimbal operation mode was an important setting for performing the SAR experiments. The yaw angle of the gimbal is directly related to the squint angle and should be tangent to the platform movement for the broadside stripmap mode SAR experiments. Thus, the gimbal was operated at a fixed angle parallel to the heading, while maneuvering the platform tangent to the heading.

(a)

(b)

FIGURE 5. **Picture of the radar system. Image (a) shows a picture of the plastic case, three stacked boards, and the radar system, and (b) is a picture of the SAR system mounted on the platform.**

The tablet was also used to maneuver the platform with an autopilot function using the DJI GS Pro application provided by DJI [44]. In the application, a set of waypoints with longitude, latitude, height, velocity, and heading information is used to fly the aircraft at specific flight paths. The latitude and longitude of the flight path were obtained using Google Earth software from Google. The heading angle, which governs the squint angle in the developed SAR system, was calculated according to the longitude and latitude of the flight path using Mapping Toolbox of Matlab from Mathworks.

Overall, a W-band SAR system mounted on a multirotor UAV with a single transmit channel and two receive channels capable of real-time data transmission was assembled. The radar module was capable of transmitting a W-band signal with 1 GHz bandwidth and over 20 dBm power, and the maximum range according to the sampling rate was 180 m. Operation time of the SAR system bounded by the maximum platform operation time was 15 minutes.

III. DRONE SAR EXPERIMENT RESULTS

A. DATA ACQUISITION FROM THE DEVELOPED DRONE SAR SYSTEM

To test the imaging performance of the system, SAR experiments were conducted on campus. Considering the radar maximum range, the platform was flown 30 *m* above the target with a 73° depression angle, illuminating the target at a 100 *m* ground range. The ground station was placed near the flight path to conserve the platform battery, where one person controlled the platform using the remote controller, and another person controlled the radar using the control PC.

Before platform takeoff, the connection between the radar and control PC was confirmed by connecting to the radar using TeraTerm, an open-source terminal program. After taking off and starting autopilot, the platform moved to the start position of the flight course. When the person controlling the platform demonstrated that the platform was on the experimental flight track, the person controlling the radar activated the network function of the radar. Thereafter, radar signals from different azimuth positions were stored into the control PC until the platform reached the end of the flight track.

The radar was operated using a PRI value of 2 *ms*, which corresponds to 500 *Hz* of PRF, to safely store the pulses. Unlike TCP, UDP does not guarantee that the packet will arrive at the destination. If one out of the four packets that consist a single pulse fails to arrive at the control PC, the data conversion software program fails to generate a data file. The loss of a packet is inevitable and may be severe if an interference occurs between the datalink antennas or if the datalink antennas are not properly facing each other. Thus, to minimize the pack loss, PRI was chosen to be larger than the pulse length.

B. SIGNAL PROCESSING

In our research, MATLAB software was used to process the data acquired from the Drone SAR system. The data preprocessing and signal processing steps are shown in Figure 6. A MATLAB script to parse individual data files and to convert them into MATLAB variables was developed. The parsing script iteratively opened the data files to generate a data matrix organized in $slow-time \times fast-time$ and an auxiliary variable containing the differential slow-time variable. Then, the differential slow time was compared to the actual PRI used for the measurement to identify any pulse data that failed to be stored. The absent pulses must be adequately interpolated to apply general SAR algorithms that assume uniform sampling in slow-time. Empirically, as long as the two datalink antennas are facing each other and there is no interference between them, a zero-array inserted at the location of the absent pulse was sufficient to apply general SAR algorithms.

Numerous algorithms such as the range migration algorithm (RMA), polar formatting algorithm (PFA), backprojection, and chirp scaling algorithm can be used to generate the SAR image [45]–[47]. In our research, RMA was used to synthesize the image of the target. The phase corrected data are Fourier transformed to the spatial frequency domain and is multiplied by a matched filter. Thereafter, Stolt interpolation is performed to correct the range migration, and two dimensional inverse Fourier transformation is applied to generate the SAR image.

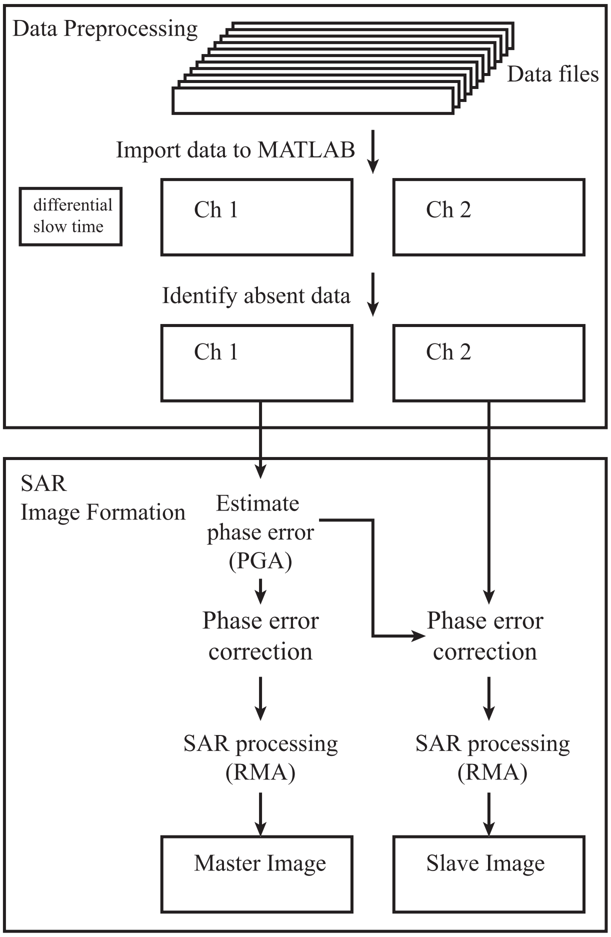

FIGURE 6. **Flowchart of the Drone SAR System data signal processing.**

The instability of the platform causes deviations from a nominal track. The deviation manifests as phase error in the radar signal. To compensate the phase error, the deviation from the nominal track can be measured and the phase error can be calculated [48]. The accuracy of the platform movement must be smaller than the wavelength of the transmitted frequency, and the information must be provided every PRI, which is not realistic when using a millimeter wave. As an alternative approach, the phase error can be calculated directly from the raw data using autofocus algorithms. In our research, the phase gradient algorithm (PGA) was used to iteratively calculate the phase error for each pulse, which is used to correct the data [49]–[52]. For a rigidly connected antenna, phase error due to non-ideal motion is common to each channel, thus phase error calculated using Ch1 data was used to compensate the motion error for both channels [53].

C. MEASUREMENTS FROM ARTIFICIAL STRUCTURES

To test the functionality of the developed system in realistic scenarios, experiments were conducted using artificial structures at Yonsei University. An optical image of the campus captured from Google Earth is shown in Figure 7. For convenient interpretation of the radar image, structures that were

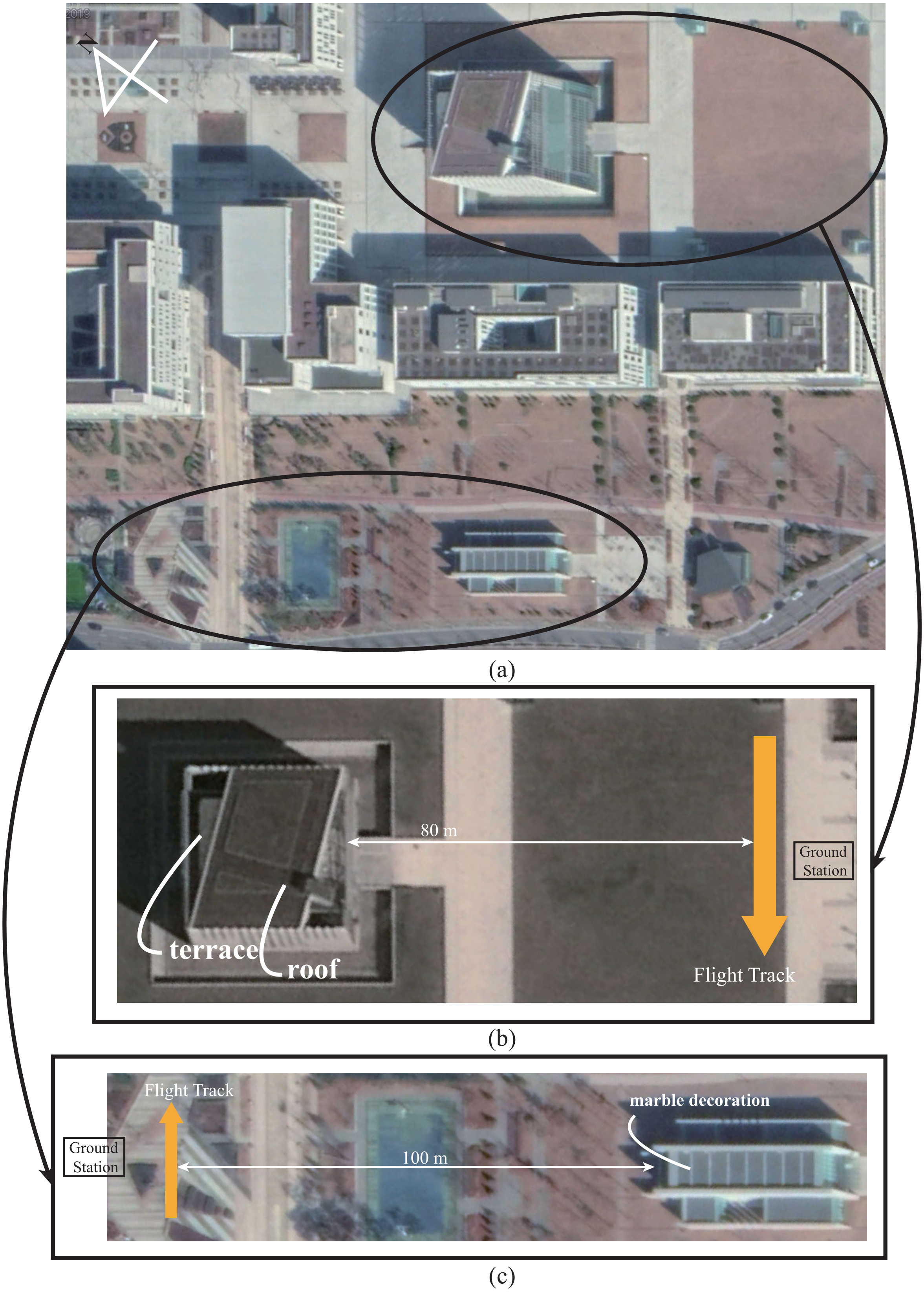

FIGURE 7. Picture of the experiment scene. Image (a) is an optical image of the experiment scene captured from GoogleEarth; (b) is an enlarged image of the library with the location of the platform flight track and the ground station, and (c) is an enlarged image of the chapel with the location of the platform flight track and the ground station.

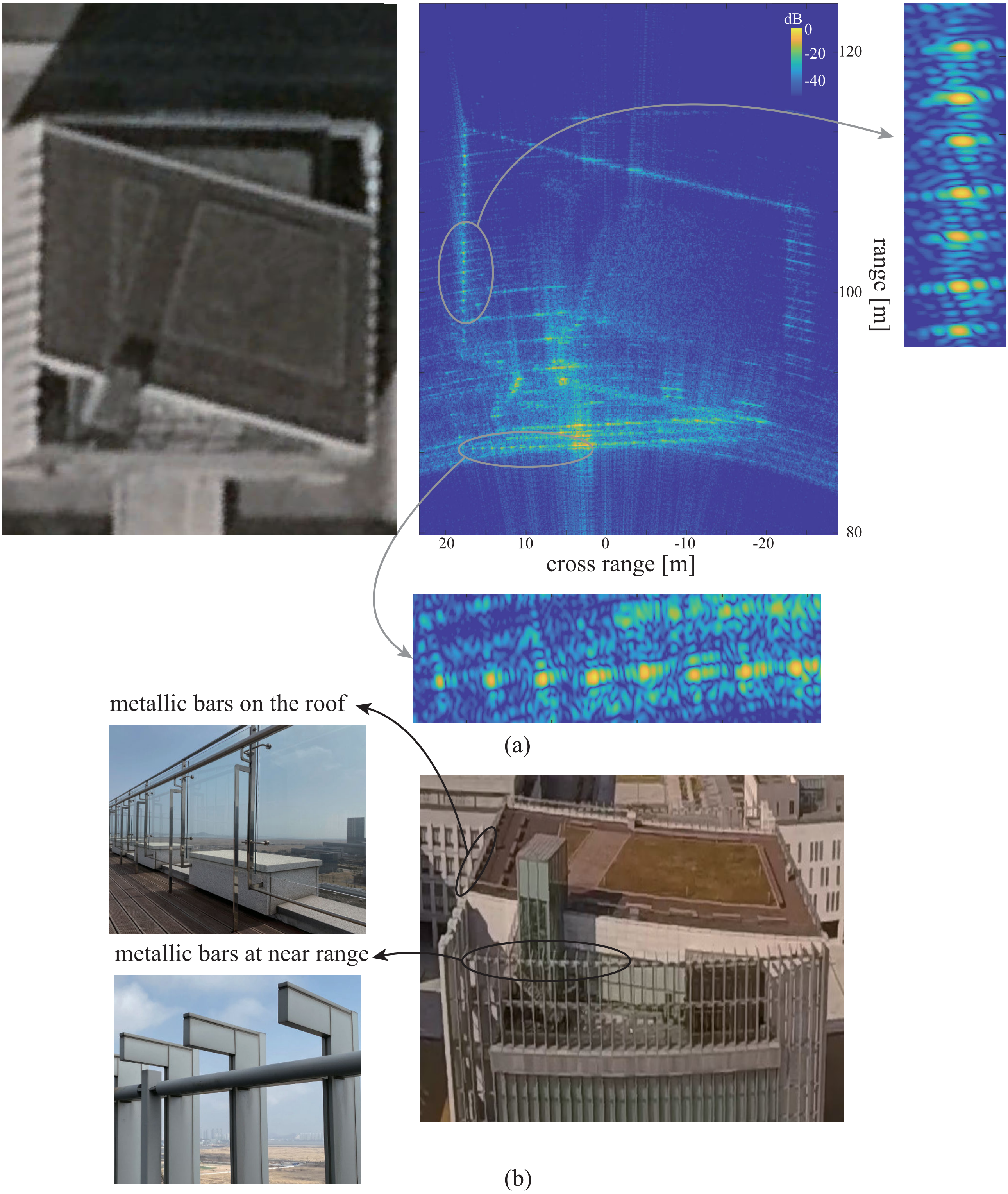

FIGURE 8. Imaging result of the library experiment. Image (a) is a SAR image processed with RMA, and (b) shows an Optical image of the library taken from the same height as the SAR measurement and two pictures taken from the roof of the library.

isolated and have a distinguishable structure were chosen for the experiment target. Therefore, the Underwood Memorial Library and the Christine Chapel were chosen as the target.

The flight track and geometry of the library experiment are shown in Figure 7 (b). The platform was flown over a lawn in front of the library. The library height was 36 *m*;

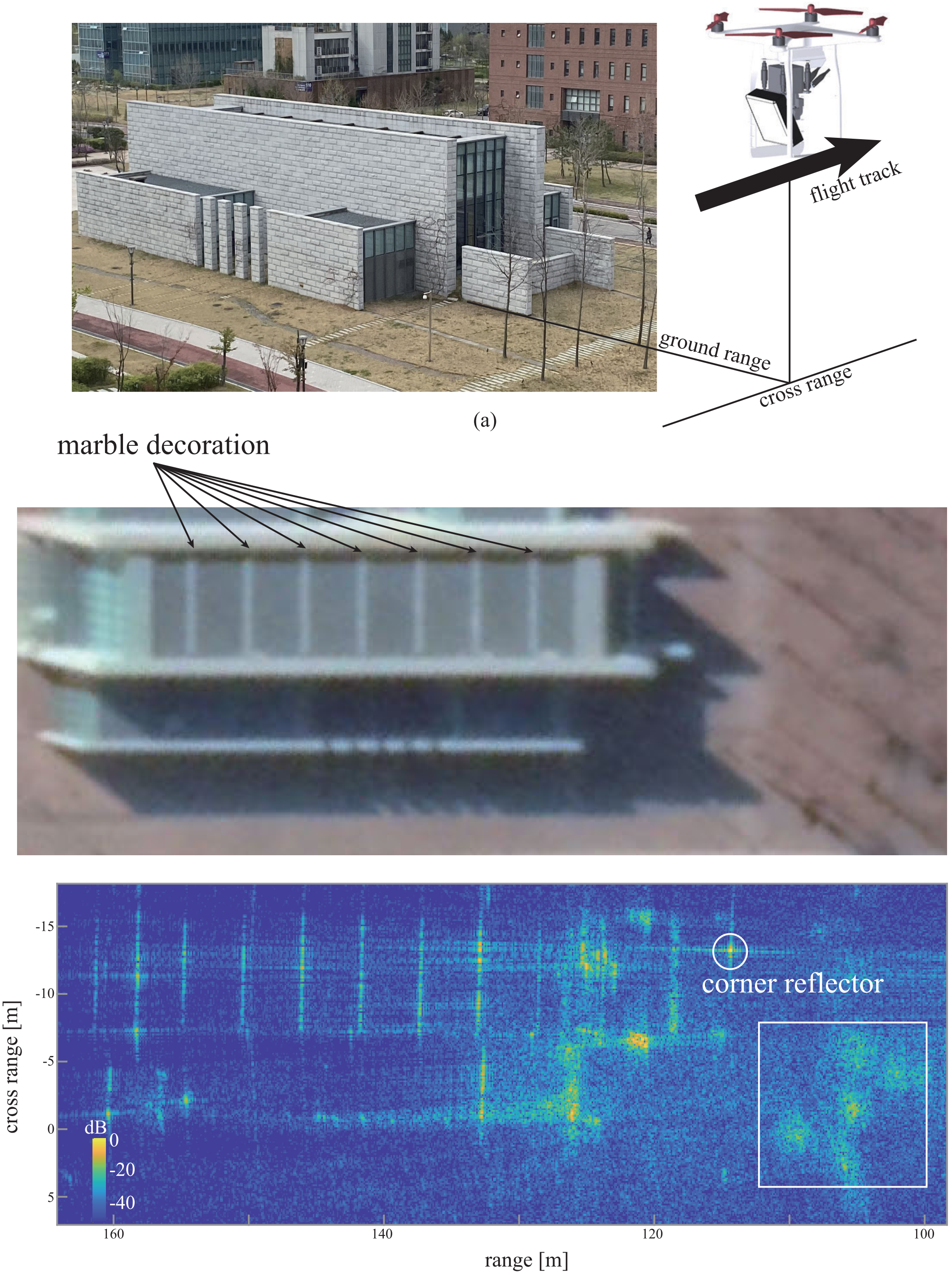

(a)

(b)

FIGURE 9. Imaging result of the chapel experiment. Image (a) is an optical image of the building, and (b) shows a SAR image processed with RMA.

thus, the platform was flown 66 *m* above ground to maintain the same depression angle. The rectangular parallel-piped structure is eight floors high, where the eighth floor (roof floor) is made of wooden ground with grass areas. A portion of the seventh floor is used as a terrace; thus, the building seen from the top looks like a rectangle with a parallelogram inside. The walls of the library are made of concrete with four sides, and the wall facing the radar had another outer layer made of metallic bars stacked in the azimuth direction.

The resultant radar image of the library experiment is shown in Figure 8. The rectangular structure of the outer walls and the border between the terrace and roof can be observed. The metallic bars of the wall facing the radar are magnified and are shown in Figure 8 (b) as well as a picture taken from the roof of the library. The reflection from the metallic bars separated in azimuth with a distance of 1 m is shown in the radar image as point-scatterer-like responses along the same range bin. The average distance between the local maximum of the image is 1.1 m, which corresponds to the distance between the metallic bars. Multiple point-scatterer like responses are also present along the same azimuth bin at the location corresponding to the upper edge of the building, magnified in Figure 8. This response is owing to the regularly spaced metallic bars placed on the edge of the roof floor for safety.

The flight track and geometry of the chapel experiment are shown in Figure 7 (c). The chapel building looks like three long rectangular boxes attached along the long edge. The surface of the building consists of marble, and the roof of the building is decorated with marbles. In front of the building are grass areas with trees. A corner reflector with an radar cross section (RCS) of 30 m^2 was placed in front of the building to assess the imaging quality.

The resultant radar image of the chapel experiment is shown in Figure 9, where (a) is an optical image taken from approximately same height as the platform and (b) is the synthesized SAR image. High reflection from the edge of the building shows the overall structure of the target. The marble decoration on the roof of the building is also visible as vertical lines at the location of the building roof. The point target response in the near range of the building with a high amplitude is the reflection from the corner reflector. A vague response is present in the near range of the image that forms five clusters at the bottom of Figure 9 (b). This is the response from the trees in front of the building.

D. INTERFEROMETRIC SAR MEASUREMENTS

To show the multichannel functionalities of the developed Drone SAR system, a cross track interferometric SAR experiment was performed. By utilizing the cross track interferometric SAR measurements, the height of the illuminated scene can be obtained [20]. The Rx channel of the radar is spatially separated by 76 mm in the developed radar module, which allows a fixed baseline interferometry. The transmitted RF signals are received by the two antennas attached to the Rx ports at the same time; thus, there is no temporal decorrelation between the signals from the two channels. In addition, because of the short baseline of the system, the image co-registration process is not required. The image co-registration process requires complex signal processing, such as mesh transformation and back geo-coding, thus, high quality interferogram can be obtained using the developed system with minimal signal processing effort.

Figure 10 shows the geometry of the cross-track interferometric SAR experiment where A_1 and A_2 are the antenna phase center (APC) of the master and slave channels, respectively [54]. The APC of the master channel is the mid-point between the Tx antenna and the antenna attached to Rx port 1, and the APC of the slave channel is the mid-point between the Tx antenna and the antenna attached to Rx port 2. The distance between A_1 and A_2 is B, and the height of A_1 is h_0. Considering a target at ground range y and height h_0, the range between the target and A_1 is denoted as r_1, and the range between the target and A_2 is denoted as r_2. The ground range of a point on the ground that satisfies $r_{01} = r_1$ is y_0, and the range from that point to A_2 is r_{02}. The angle between the $z-$axis and r_1 is θ, and the angle between the $z-$ axis and r_{01} is θ_0. A corner reflector with RCS 100 m^2 placed on a flat ground was used as the target scene for the interferometric SAR measurement. Table 3 lists the parameters used for the interferometric SAR measurement. The height h_0 was chosen so that the platform was within the visible range for safety. The depression angle α was chosen to keep the scene center at the range of the system requirements.

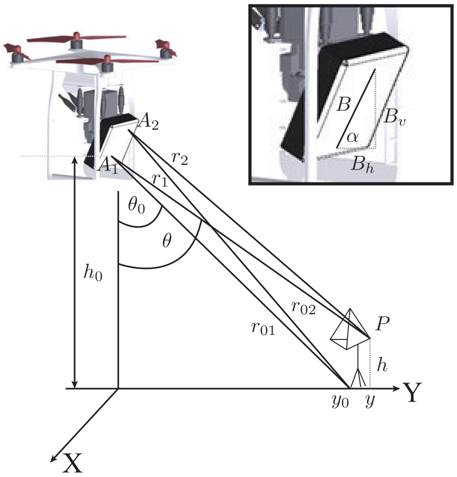

FIGURE 10. Geometry of InSAR measurement.

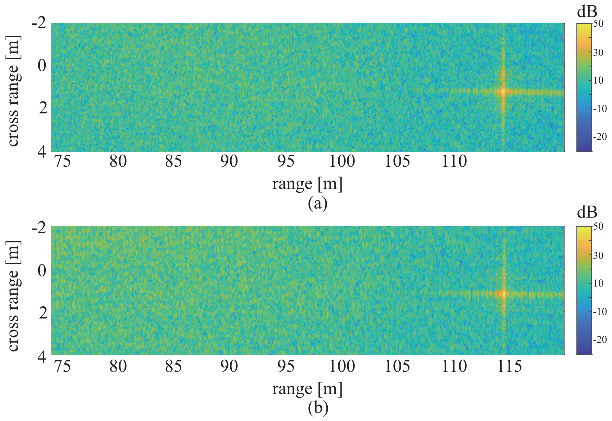

FIGURE 11. Reconstructed SAR Image from two channels. Image (a) is the master image from Rx port 1, and (b) is the slave image from Rx port 2.

The interferogram can be generated by utilizing the two complex images reconstructed from the different

TABLE 3. Geometric parameters of the interferometric SAR measurement.

parameter	units	value
h_0	m	30
r_1	m	115
B	cm	3.8
α	°	73
h	m	1

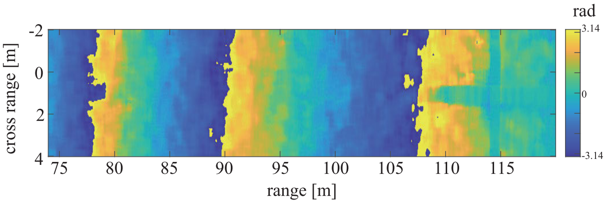

FIGURE 12. Interferogram generated from InSAR product.

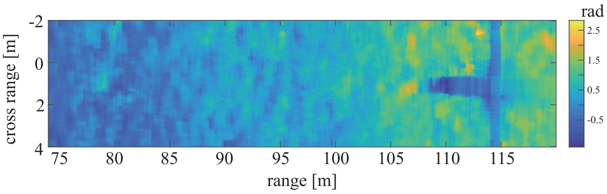

FIGURE 13. Initial topographic phase map.

Rx channels. The two SAR images produced using PGA and RMA are shown in Figure 11. A strong response from the corner reflector is visible at range 115 *m*. To generate the interferogram, the master image and complex conjugate of the slave image is multiplied pixel by pixel to generate an InSAR product. Then, the angle operator is taken to the InSAR product to obtain the phase values of the InSAR product, resulting in an interferogram. The InSAR sensor is a sensitive sensor; thus, a noise reduction filter is usually applied in realistic systems. In our research, a square moving average filter with a width of 75 *cm* (approximately five times the resolution) was used prior to the angle operator. The resultant interferogram is shown in Figure 12.

Each phase value that contains the interferogram is a sum of multiple elements, shown in (2), where ϕ denotes a phase value of an InSAR product. The displacement phase, denoted as ϕ_{disp} in (2), occurs owing to the displacement of the illuminated scene between the measurement times of the master image and slave image. Thus, displacement phase may be significant when performing repeat-pass interferometric measurements, however, it is considered negligible for single-pass measurements. The topographic phase, denoted as ϕ_{topo} in (2), occurs owing to the topographic characteristics of the terrain and can be used to measure the relative height of the illuminated scene.

$$\phi = \phi_{gnd} + \phi_{topo} + \phi_{disp} \tag{2}$$

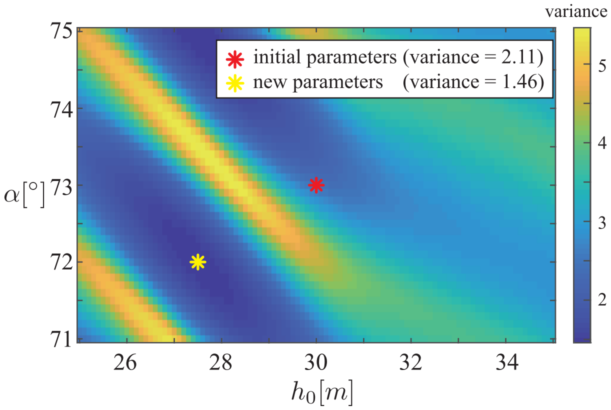

FIGURE 14. Variance of interferogram calculated for different antenna heights and grazing angles.

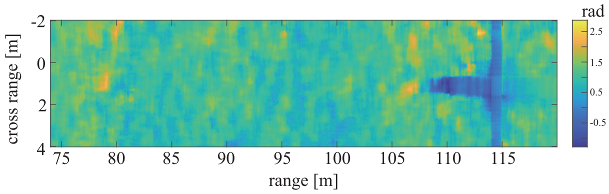

FIGURE 15. Topographic phase map generated with new parameters.

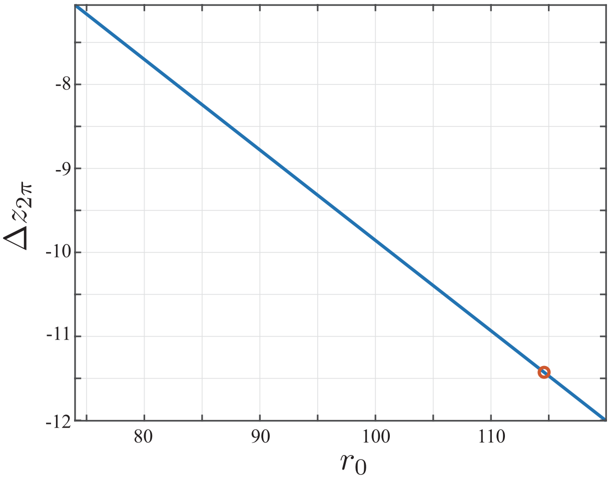

FIGURE 16. Ambiguous height calculated for different ranges.

The ground phase, denoted ϕ_{gnd} in (2), is the most dominant element that contributes to the interferogram. The ground phase is the contribution from the ground that manifests itself as fringe patterns along the range direction in the interferogram. To obtain topographic information from the interferogram, the ground phase should be removed. The ground phase can be removed using a digital elevation model (DEM) of the scene or by mathematically modeling the phase of the ground. In our research, the latter method was utilized. Considering the low altitude of the measurement platform, the ground can be approximated as flat earth. The resultant model of the ground phase is expressed

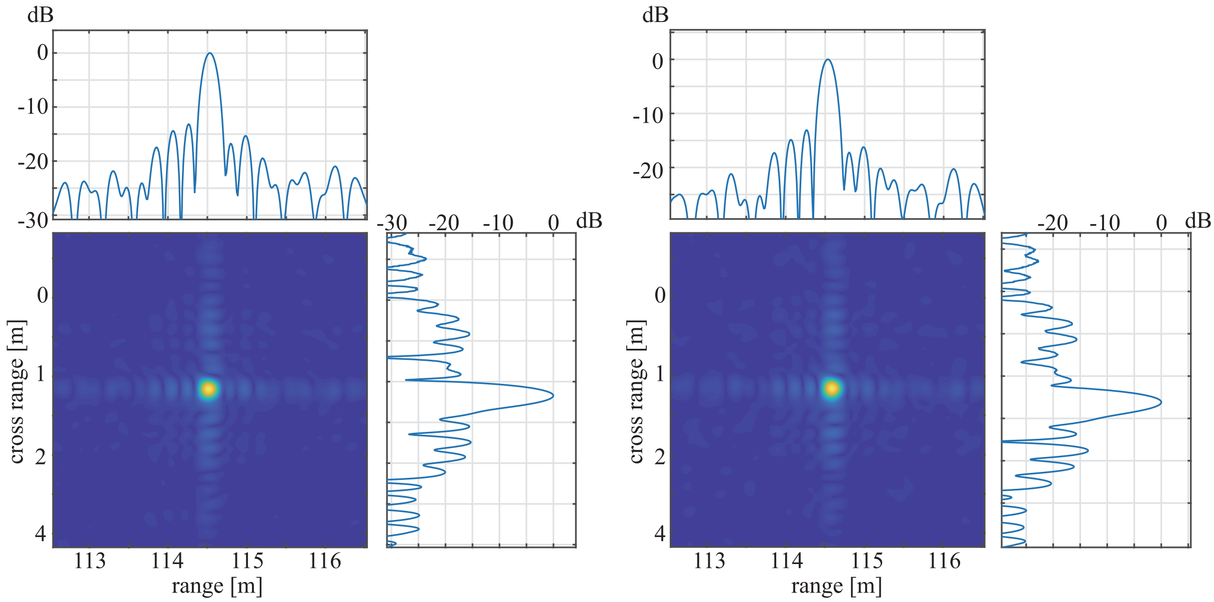

(a) (b)

FIGURE 17. **Enlarged SAR image, range profile, and cross range profile of the target: (a) Rx 1 and (b) Rx 2.**

as (3).

$$\phi_{flat} = \frac{4\pi}{\lambda}(r_{02}-r_{01}) = \frac{4\pi}{\lambda}\left(r_1\sqrt{1+\frac{B^2-2r_1B\sin\theta_0-\alpha}{r_1^2}}-r_1\right) \quad (3)$$

The ground phase can be removed from the interferogram by subtracting the ground phase calculated for different r_1 using (3), resulting in a topographic phase map. The resultant topographic phase map is shown in Figure 13, where two major observations can be made. First, the value of the topographic phase gradually increases as the range increases. Second, a cross-shaped discontinuity is present at the location of the corner reflector.

The second phenomenon is owing to the response from the corner reflector with a high RCS displaced from the ground. Thus, the phase at the middle of the cross shape is considered the topographic phase of the target. The discontinuous phase values outside the intersection of the cross shape are a result of the topographic phase of the target subtracted by the ground phase of the clutter, which can result in an erroneous interpretation of the topographic phase. This phenomenon can be reduced using sidelobe suppressing windows; however it is inevitable when there is a target with a high RCS within the scene.

The first phenomenon contradicts the preconditions made on the illuminated scene because gradually increasing topographic phase implies a downward slope with an increasing range. This phenomenon is the result of insufficient removal of the of ground phase. Because of the characteristics of the UAV platform, the platform could move in a geometry different from the intended one. In this case, the ground phase is not properly modeled because erroneous geometric parameters were used for the modeling. Thus, a method to extract the exact geometric parameters of the measurement is required.

To determine the exact geometric parameters of the measurement, the variance of the topographic phase map was used. The topographic phase of flat ground is constant; thus, the variance of the topographic map is expected to be zero. Assuming that the baseline tilt angle α and height of the platform h_0 may be erroneous, multiple topographic phase maps were generated using different values of α and h_0, and their variances were calculated. Figure 14 shows the variance calculated for topographic phase maps generated using different values of α and h_0. Figure 14 shows pairs of (α, h_0) values that may result in a more constant topographic phase map generated using the initial geometric parameters of $(73^\circ, 30\ m)$. Thus, a (α, h_0) pair that results in a local minimum in Figure 14 was considered a more realistic geometric parameter.

The topographic phase map was generated using the new geometric parameters of $\alpha = 72.2^\circ$ and $h_0 = 27.5$ and is shown in Figure 15. Compared to Figure 13, the phase of the clutter is constant for different ranges, and discontinuity between the target response is present. Thus, Figure 15 is considered more adequate for interpretation.

The topographic phase can be converted to the height of the terrain using an ambiguous height $\Delta z_{2\pi}$, which is the height of the terrain that induces the topographic phase of 2π. The relationship between the ambiguous height and range is given in (4), where $B_\perp$ is the perpendicular baseline $B_\perp = B\cos(\theta_0 - \alpha)$. Thus, the ambiguous height for the different

TABLE 4. **Image performance parameters.**

		resolution	PSLR	ISLR
Ch 1	range	$0.1692\ m$	$-13.26\ dB$	$-12.25\ dB$
	cross range	$0.1667\ m$	$-15.29\ dB$	
Ch 2	range	$0.1705\ m$	$-13.11\ dB$	$-12.64\ dB$
	cross range	$0.1709\ m$	$-15.55\ dB$	

range can be calculated using the geometric parameters of the InSAR measurement, which is shown in Figure 16.

$$\Delta z_{2\pi} = -\frac{\lambda r_1 \sin\theta_0}{B_\perp} \tag{4}$$

The height of the terrain is related to the topographic phase by (5). The ambiguous height of the range corresponding to the target location is $-11.42\ m$, and the measured topographic phase relative to the clutter is $-1.0289\ rad$. The resultant height calculated by (5) is $h = 0.9357\ m$.

$$\phi_{topo} = \frac{4\pi}{\Delta z_{2\pi}} h \tag{5}$$

E. IRF MEASUREMENT

To further analyze the imaging capabilities of the Drone SAR system, impulse response function (IRF) of the system was obtained by extracting the target response from Figure 11. The extracted IRF from the two channels are shown in Figure 17, where two 2-D sinc functions are obtained.

The image performance parameters, such as resolution, peak sidelobe ratio (PSLR), and integrated sidelobe ratio (ISLR), are measured from Figure 17 and are listed in Table 4. The centimeter level resolution and adequate level of the sidelobes shows the validity of the developed system for use in small scale radar imaging of the illuminated scene using multirotor UAVs as platforms.

IV. CONCLUSION

In this paper multichannel SAR system mounted on a multirotor UAV platform capable of real-time data transmission is presented. The radar system is developed using commercial millimeter-wave mmICs, digital boards, and communication modules with small and lightweight characteristics. The lightweight radar can be mounted on a multirotor UAV, which can be used to generate SAR images.

The developed SAR system is composed of three subsystems; the UAV platform, radar module, and ground station. A hexarotor UAV from DJI was chosen for the platform to carry the radar module. The selected platform is capable of carrying a payload up to 10 *kg* and can operate with predesignated navigational data. The radar module used 77 *GHz* as the center frequency, and the transmit power was measured to be 23 *dBm* for high resolution imaging with a small size and weight. The radar module also included datalinks, and the radar data was captured in real-time. The ground station remotely controlled the radar module and platform, allowing SAR data acquisition using a drone.

The functionality of the Drone SAR system was verified by field tests. The radar imaging capability of the developed system was verified by illuminating artificial buildings and applying SAR algorithms to the received data. The structure and location of the illuminated buildings and trees were acquired. The multichannel capabilities of the developed system were verified by illuminating a corner reflector of a known height. After interferometric processing of the images received from the two channels, the height of the target was retrieved.

These results demonstrate the promising application of radars mounted on drones for disaster monitoring, remote sensing, and agriculture. The multichannel characteristic can be used for topographic mapping with a shorter revisit time than that of other platforms. In the future, application of real-time SAR algorithms and interferometry will be studied to obtain InSAR images in real-time using the proposed SAR system. Also, advanced motion compensation method for SAR interferometry will be considered for accurate interferometric processing.

REFERENCES

[1] H. Shakhatreh, A. H. Sawalmeh, A. Al-Fuqaha, Z. Dou, E. Almaita, I. Khalil, N. S. Othman, A. Khreishah, and M. Guizani, "Unmanned aerial vehicles (UAVs): A survey on civil applications and key research challenges," *IEEE Access*, vol. 7, pp. 48572–48634, 2019.

[2] C. Zhang and J. M. Kovacs, "The application of small unmanned aerial systems for precision agriculture: A review," *Precis. Agricult.*, vol. 13, no. 6, pp. 693–712, Dec. 2012.

[3] J. A. Gonçalves and R. Henriques, "UAV photogrammetry for topographic monitoring of coastal areas," *ISPRS J. Photogramm. Remote Sens.*, vol. 104, pp. 101–111, Jun. 2015. [Online]. Available: http://www.sciencedirect.com/science/article/pii/S0924271615000532

[4] D. Leary, "Drones on ice: An assessment of the legal implications of the use of unmanned aerial vehicles in scientific research and by the tourist industry in Antarctica," *Polar Rec.*, vol. 53, no. 4, p. 343–357, 2017.

[5] A. Bhardwaj, L. Sam, Akanksha, F. J. Martín-Torres, and R. Kumar, "UAVs as remote sensing platform in glaciology: Present applications and future prospects," *Remote Sens. Environ.*, vol. 175, pp. 196–204, Mar. 2016. [Online]. Available: http://www.sciencedirect.com/science/article/pii/S0034425715302509

[6] C. Gomez and H. Purdie, "UAV-based photogrammetry and geocomputing for hazards and disaster risk monitoring–a review," *Geoenviron. Disasters*, vol. 3, p. 23, Nov. 2016.

[7] J. Elston, B. Argrow, M. Stachura, D. Weibel, D. Lawrence, and D. Pope, "Overview of small fixed-wing unmanned aircraft for meteorological sampling," *J. Atmos. Ocean. Technol.*, vol. 32, no. 1, pp. 97–115, Jan. 2015, doi: 10.1175/JTECH-D-13-00236.1.

[8] T.-Z. Xiang, G.-S. Xia, and L. Zhang, "Mini-unmanned aerial vehicle-based remote sensing: Techniques, applications, and prospects," *IEEE Geosci. Remote Sens. Mag.*, vol. 7, no. 3, pp. 29–63, Sep. 2019.

[9] I. Colomina and P. Molina, "Unmanned aerial systems for photogrammetry and remote sensing: A review," *ISPRS J. Photogramm. Remote Sens.*, vol. 92, pp. 79–97, Jun. 2014. [Online]. Available: http://www.sciencedirect.com/science/article/pii/S0924271614000501

[10] P. Horstrand, R. Guerra, A. Rodriguez, M. Diaz, S. Lopez, and J. F. Lopez, "A UAV platform based on a hyperspectral sensor for image capturing and on-board processing," *IEEE Access*, vol. 7, pp. 66919–66938, 2019.

[11] P. Hugler, F. Roos, M. Schartel, M. Geiger, and C. Waldschmidt, "Radar taking off: New capabilities for UAVs," *IEEE Microw. Mag.*, vol. 19, no. 7, pp. 43–53, Nov. 2018.

[12] P. Hugler, M. Geiger, and C. Waldschmidt, "77 GHz radar-based altimeter for unmanned aerial vehicles," in *Proc. IEEE Radio Wireless Symp. (RWS)*, Jan. 2018, pp. 129–132.

[13] W. Liu, C. Yu, X. Wang, Y. Zhang, and Y. Yu, "The altitude hold algorithm of UAV based on millimeter wave radar sensors," in *Proc. 9th Int. Conf. Intell. Hum.-Mach. Syst. Cybern. (IHMSC)*, vol. 1, Aug. 2017, pp. 436–439.

[14] M. Schartel, R. Burr, P. Schoeder, G. Rossi, P. Hugler, W. Mayer, and C. Waldschmidt, "Radar-based altitude over ground estimation of UAVs," in *Proc. 11th German Microw. Conf. (GeMiC)*, Mar. 2018, pp. 103–106.

[15] A. Moses, M. J. Rutherford, M. Kontitsis, and K. P. Valavanis, "UAV-borne X-band radar for collision avoidance," *Robotica*, vol. 32, no. 1, pp. 97–114, 2014.

[16] R. O. R. Jenssen, M. Eckerstorfer, and S. Jacobsen, "Drone-mounted ultrawideband radar for retrieval of snowpack properties," *IEEE Trans. Instrum. Meas.*, vol. 69, no. 1, pp. 221–230, Jan. 2020.

[17] K. Wu, G. A. Rodriguez, M. Zajc, E. Jacquemin, M. Clément, A. De Coster, and S. Lambot, "A new drone-borne GPR for soil moisture mapping," *Remote Sens. Environ.*, vol. 235, Dec. 2019, Art. no. 111456. [Online]. Available: http://www.sciencedirect.com/science/article/pii/S0034425719304754

[18] A. Moreira, P. Prats-Iraola, M. Younis, G. Krieger, I. Hajnsek, and K. P. Papathanassiou, "A tutorial on synthetic aperture radar," *IEEE Geosci. Remote Sens. Mag.*, vol. 1, no. 1, pp. 6–43, Mar. 2013.

[19] A. Reigber, R. Scheiber, M. Jager, P. Prats-Iraola, I. Hajnsek, T. Jagdhuber, K. P. Papathanassiou, M. Nannini, E. Aguilera, S. Baumgartner, R. Horn, A. Nottensteiner, and A. Moreira, "Very-High-Resolution airborne synthetic aperture radar imaging: Signal processing and applications," *Proc. IEEE*, vol. 101, no. 3, pp. 759–783, Mar. 2013.

[20] P. A. Rosen, S. Hensley, I. R. Joughin, F. K. Li, S. N. Madsen, E. Rodriguez, and R. M. Goldstein, "Synthetic aperture radar interferometry," *Proc. IEEE*, vol. 88, no. 3, pp. 333–382, Mar. 2000.

[21] S. Hensley, K. Wheeler, and G. Sadowy, "The UAVSAR instrument: Description and first results," in *Proc. IEEE Radar Conf.*, May 2008, pp. 1–6.

[22] M. Edrich, "Ultra-lightweight synthetic aperture radar based on a 35 GHz FMCW sensor concept and online raw data transmission," *IEE Proc. Radar, Sonar Navigat.*, vol. 153, no. 2, pp. 129–134, Apr. 2006.

[23] H. Essen, W. Johannes, S. Stanko, R. Sommer, A. Wahlen, and J. Wilcke, "High resolution W-band UAV SAR," in *Proc. IEEE Int. Geosci. Remote Sens. Symp.*, Jul. 2012, pp. 5033–5036.

[24] H. W. Schulz, "The unmanned mission avionics test Heliciopter-a flexible and versatile Vtol-Uas experimental system," *ISPRS-Int. Arch. Photogramm., Remote Sens. Spatial Inf. Sci.*, vol. 3822, pp. 309–314, Sep. 2011.

[25] S. N. Madsen, S. Hensley, K. Wheeler, G. A. Sadowy, T. Miller, R. Muellerschoen, Y. Lou, and P. A. Rosen, "UAV-based L-band SAR with precision flight path control," in *Enabling Sensor and Platform Technologies for Spaceborne Remote Sensing*, vol. 5659, G. J. Komar, J. Wang, and T. Kimura, Eds. Bellingham, WA, USA: SPIE, 2005, pp. 51–60. [Online]. Available: https://doi.org/10.1117/12.578373

[26] L. Moreira, F. Castro, J. A. Goes, L. Bins, B. Teruel, J. Fracarolli, V. Castro, M. Alcantara, G. Ore, D. Luebeck, L. P. Oliveira, L. Gabrielli, and H. E. Hernandez-Figueroa, "A drone-borne multiband DInSAR: Results and applications," in *Proc. IEEE Radar Conf. (RadarConf)*, Apr. 2019, pp. 1–6.

[27] M. Lort, A. Aguasca, C. Lopez-Martinez, and T. M. Marin, "Initial evaluation of SAR capabilities in UAV multicopter platforms," *IEEE J. Sel. Topics Appl. Earth Observ. Remote Sens.*, vol. 11, no. 1, pp. 127–140, Jan. 2018.

[28] W. K. Lee and K. W. Lee, "Experimental operation of drone micro-SAR with efficient time-varying velocity compensation," *Electron. Lett.*, vol. 53, no. 10, pp. 682–683, May 2017.

[29] M. G. Fernandez, Y. A. Lopez, A. A. Arboleya, B. G. Valdes, Y. R. Vaqueiro, F. Las-Heras Andres, and A. Pino Garcia, "Synthetic aperture radar imaging system for landmine detection using a ground penetrating radar on board a unmanned aerial vehicle," *IEEE Access*, vol. 6, pp. 45100–45112, 2018.

[30] G. Ludeno, I. Catapano, A. Renga, A. R. Vetrella, G. Fasano, and F. Soldovieri, "Assessment of a micro-UAV system for microwave tomography radar imaging," *Remote Sens. Environ.*, vol. 212, pp. 90–102, Jun. 2018. [Online]. Available: http://www.sciencedirect.com/science/article/pii/S0034425718301974

[31] J. Yan, J. Guo, Q. Lu, K. Wang, and X. Liu, "X-band mini SAR radar on eight-rotor mini-UAV," in *Proc. IEEE Int. Geosci. Remote Sens. Symp. (IGARSS)*, Jul. 2016, pp. 6702–6705.

[32] G. Zhou, "Near real-time orthorectification and mosaic of small UAV video flow for time-critical event response," *IEEE Trans. Geosci. Remote Sens.*, vol. 47, no. 3, pp. 739–747, Mar. 2009.

[33] J. Hasch, E. Topak, R. Schnabel, T. Zwick, R. Weigel, and C. Waldschmidt, "Millimeter-wave technology for automotive radar sensors in the 77 GHz frequency band," *IEEE Trans. Microw. Theory Techn.*, vol. 60, no. 3, pp. 845–860, Mar. 2012.

[34] (2020). *Matrice 600 Pro*. [Online]. Available: https://www.dji.com/matrice600-pro/info

[35] (2020). *Ronin MX*. [Online]. Available: https://www.dji.com/ronin-mx/info

[36] (2020). *D-RTK*. [Online]. Available: https://www.dji.com/d-rtk/info

[37] (2020). *A3 Pro*. [Online]. Available: https://www.dji.com/uk/a3/info

[38] (2020). *Lightbridge*. [Online]. Available: https://www.dji.com/lightbridge-2/info

[39] S.-Y. Jeon, S. Kim, J. Kim, S. Kim, S. Shin, M. Kim, and M.-H. Ka, "W-band FMCW MIMO radar system for high-resolution multimode imaging with Time- and frequency-division multiplexing," *IEEE Trans. Geosci. Remote Sens.*, vol. 58, no. 7, pp. 5042–5057, Jul. 2020.

[40] S.-Y. Jeon, M.-H. Ka, S. Shin, M. Kim, S. Kim, S. Kim, J. Kim, A. Dewantari, J. Kim, and H. Chung, "W-band MIMO FMCW radar system with simultaneous transmission of orthogonal waveforms for high-resolution imaging," *IEEE Trans. Microw. Theory Techn.*, vol. 66, no. 11, pp. 5051–5064, Nov. 2018.

[41] AVNET. (2020). *Picozed*. [Online]. Available: https://www.avnet.com/opasdata/d120001/medias/docus/187/5048-PB-PDP-AES-Z7PZ-SOM-G-V2.pdf

[42] Xilinx. (2020). *Zynq7000*. [Online]. Available: https://www.xilinx.com/support/documentation/data_sheets/ds190-zynq-7000-overview.pdf

[43] (2020). *Dji Go*. [Online]. Available: https://www.dji.com/uk/goapp

[44] (2020). *Dji GS Pro*. [Online]. Available: https://www.dji.com/uk/ground-station-pro

[45] W. Carrara, W. Carrara, R. Goodman, and R. Majewski, *Spotlight Synthetic Aperture Radar: Signal Processing Algorithms Artech House Remote Sensing Library*. Norwood, MA, USA: Artech House, 1995. [Online]. Available: https://books.google.co.kr/books?id=uztiQgAACAAJ

[46] P. Thompson, D. E. Wahl, P. H. Eichel, D. C. Ghiglia, and C. V. Jakowatz, *Spotlight-Mode Synthetic Aperture Radar: A Signal Processing Approach*. Norwell, MA, USA: Kluwer, 1996.

[47] M. Soumekh, *Synthetic Aperture Radar Signal Processing with MATLAB Algorithms*. Hoboken, NJ, USA: Wiley, 1999.

[48] R. Wang, Y.-H. Luo, Y.-K. Deng, Z.-M. Zhang, and Y. Liu, "Motion compensation for high-resolution automobile FMCW SAR," *IEEE Geosci. Remote Sens. Lett.*, vol. 10, no. 5, pp. 1157–1161, Sep. 2013.

[49] D. E. Wahl, P. H. Eichel, D. C. Ghiglia, and C. V. Jakowatz, "Phase gradient autofocus–A robust tool for high resolution SAR phase correction," *IEEE Trans. Aerosp. Electron. Syst.*, vol. 30, no. 3, pp. 827–835, Jul. 1994.

[50] P. H. Eichel and C. V. Jakowatz, "Phase-gradient algorithm as an optimal estimator of the phase derivative," *Opt. Lett.*, vol. 14, no. 20, pp. 1101–1103, 1989.

[51] H. Lim Chan and T. Soon Yeo, "Noniterative quality phase-gradient autofocus (QPGA) algorithm for spotlight SAR imagery," *IEEE Trans. Geosci. Remote Sens.*, vol. 36, no. 5, pp. 1531–1539, Sep. 1998.

[52] N. Li, R. Wang, Y. Deng, W. Yu, Z. Zhang, and Y. Liu, "Autofocus correction of residual RCM for VHR SAR sensors with light-small aircraft," *IEEE Trans. Geosci. Remote Sens.*, vol. 55, no. 1, pp. 441–452, Jan. 2017.

[53] D. R. Stevens, I. G. Cumming, and A. L. Gray, "Options for airborne interferometric SAR motion compensation," *IEEE Trans. Geosci. Remote Sens.*, vol. 33, no. 2, pp. 409–420, Mar. 1995.

[54] Z. Xiang, K. Wang, and X. Liu, "A Model-Spectrum-Based flattening algorithm for airborne single-pass SAR interferometry," *IEEE Geosci. Remote Sens. Lett.*, vol. 6, no. 2, pp. 307–311, Apr. 2009.

SUMIN KIM (Graduate Student Member, IEEE) received the bachelor's degree from the School of Integrated Technology, Yonsei University, South Korea, in 2016, where he is currently pursuing the Ph.D. degree. Since 2016, he has been a Graduate Student with the Radar Systems and Wave Sensing Laboratory, School of Integrated Technology, Yonsei University. He is also involved in projects for bistatic and multistatic SAR. His current interests include high resolution radar, synthetic aperture radar, and real-time radar signal processing.

SE-YEON JEON (Member, IEEE) received the B.S. and Ph.D. degrees in IT convergence technology from Yonsei University, South Korea, in 2014 and 2019, respectively. In 2019, she joined the Microwaves and Radar Institute, German Aerospace Center (DLR), Germany, where she is currently a member with the NewSpace SAR group. Her research interests include development for microwave sensors, electromagnetic wave signal processing, SAR systems, and SAR concepts.

JEONGBAE KIM (Graduate Student Member, IEEE) received the B.S.E. degree from Yonsei University, Seoul, South Korea, in 2017, where he is currently pursuing the combined master's and doctor's degree with the Radar Systems and Wave Sensing Laboratory, School of Integrated Technology. He has been participating in several projects, including small drone based SAR systems. His main academic interests include synthetic aperture radar, its motion compensation, and radar based exploration.

UI-MIN LEE received the bachelor's degree from the School of Integrated Technology, Yonsei University, South Korea, in 2019, where he is currently pursuing the M.S. degree. Since 2019, he has been a Graduate Student with the Radar Systems and Wave Sensing Laboratory, School of Integrated Technology, Yonsei University. He is also involved in projects for bistatic and multistatic SAR. His current interests include synthetic aperture radar, real-time radar signal processing, and deep learning.

SEUNGHA SHIN received the B.S., M.S., and Ph.D. degrees in electrical and electronics engineering from Kyunghee University, Seoul, South Korea, in 1992, 1994, and 2012, respectively. He is currently a Principal Engineer with U-Tel Company Ltd., Gunpo, South Korea. His current research interests include integrated circuits and systems for SAR, AESA radar, and EW field from L-band to millimeter wave.

YOUNGWOO CHOI received the B.S. degree in electrical and electronics engineering from Soonchunhayng University, Asan, South Korea, in 2006. He is currently a Principal Engineer with U-Tel Company Ltd., Gunpo, South Korea. His current research interests include integrated circuits and systems for SAR, AESA radar, and EW field from L-band to millimeter wave.

MIN-HO KA (Member, IEEE) received the B.S. and M.S. degrees in electronics engineering from Yonsei University, Seoul, South Korea, in 1989 and 1991, respectively, and the Ph.D. degree in radio engineering from the Moscow Power Engineering Institute, Moscow, Russia, in 1997. From 1997 to 2000, he was with the Agency for Defense Development, Ministry of Defense, South Korea, for the development of microwave imaging sensors and spaceborne and airborne synthetic aperture radar (SAR). From 2002 to 2010, he was a Professor with Korea Polytech University, Siheung, South Korea, where he was the Head of the Department of the Korea-Russia Industrial Technology Cooperation Centre. He was also a Chairman with the Radar Group, Korean Institute of Electromagnetic Engineering and Science. He is currently a Professor with the Radar Systems and Wave Sensing Laboratory, School of Integrated Technology, Yonsei University. His current research interests include the system design and development of microwave sensors and spaceborne and airborne SAR.

• • •